

## SUPERNOVA 1987A: A TEMPLATE TO LINK SUPERNOVAE TO THEIR REMNANTS

S. ORLANDO<sup>1</sup>, M. MICELI<sup>1,2</sup>, M. L. PUMO<sup>1,3,4</sup>, AND F. BOCCHINO<sup>1</sup><sup>1</sup> INAF—Osservatorio Astronomico di Palermo “G.S. Vaiana”, Piazza del Parlamento 1, I-90134 Palermo, Italy; [orlando@astropa.inaf.it](mailto:orlando@astropa.inaf.it)<sup>2</sup> Dip. di Fisica e Chimica, Univ. di Palermo, Piazza del Parlamento 1, I-90134 Palermo, Italy<sup>3</sup> INAF—Osservatorio Astronomico di Padova, Vicolo dell’Osservatorio 5, I-35122 Padova, Italy<sup>4</sup> INAF—Osservatorio Astrofisico di Catania, Via S. Sofia 78, I-95123 Catania, Italy

Received 2015 May 27; accepted 2015 August 6; published 2015 September 10

## ABSTRACT

The emission of supernova remnants (SNRs) reflects the properties of both the progenitor supernovae (SNe) and the surrounding environment. The complex morphology of the remnants, however, hampers the disentanglement of the two contributions. Here, we aim at identifying the imprint of SN 1987A on the X-ray emission of its remnant and at constraining the structure of the environment surrounding the SN. We performed high-resolution hydrodynamic simulations describing SN 1987A soon after the core-collapse and the following three-dimensional expansion of its remnant between days 1 and 15,000 after the SN. We demonstrated that the physical model reproducing the main observables of SN 1987A during the first 250 days of evolution also reproduces the X-ray emission of the subsequent expanding remnant, thus bridging the gap between SNe and SNRs. By comparing model results with observations, we constrained the explosion energy in the range  $1.2\text{--}1.4 \times 10^{51}$  erg and the envelope mass in the range  $15\text{--}17 M_{\odot}$ . We found that the shape of X-ray lightcurves and spectra at early epochs ( $<15$  years) reflects the structure of outer ejecta: our model reproduces the observations if the outermost ejecta have a post-explosion radial profile of density approximated by a power law with index  $\alpha = -8$ . At later epochs, the shapes of X-ray lightcurves and spectra reflect the density structure of the nebula around SN 1987A. This enabled us to ascertain the origin of the multi-thermal X-ray emission, disentangle the imprint of the SN on the remnant emission from the effects of the remnant interaction with the environment, and constrain the pre-supernova structure of the nebula.

*Key words:* hydrodynamics – instabilities – ISM: supernova remnants – shock waves – supernovae: individual (SN 1987A) – X-rays: ISM

*Supporting material:* animations

## 1. INTRODUCTION

Supernova remnants (SNRs), the leftovers of supernova (SN) explosions, are diffuse extended sources with a quite complex morphology. The general consensus is that such morphology reflects, on one hand, the physical and chemical properties of the progenitor SN and, on the other hand, the early interaction of the SN blast wave with the inhomogeneous circumstellar medium (CSM). Thus, investigating the intimate link that exists between the morphological properties of an SNR and the complex phases in the SN explosion may help to (1) trace back the structure and chemical composition of SN ejecta, and the dynamics and energetics of the SN explosion; and (2) probe the structure and geometry of the CSM, thereby mapping the final stages of the stars evolution. However, the very different time and space scales of SNe and SNRs make it difficult to study their connection in detail (e.g., Badenes et al. 2008; Ellinger et al. 2012; Yamaguchi et al. 2014; Patnaude et al. 2015).

Because of its youth and proximity, SN 1987A in the Large Magellanic Cloud offers a unique opportunity to bridge the gap between the progenitor SN and its remnant. SN 1987A was an hydrogen-rich core-collapse (CC) SN that was observed in outburst on 1987 February 23 (West et al. 1987). It occurred approximately 51.4 kpc from Earth (Panagia 1999). About 80 days after the explosion, it reached a peak apparent visual magnitude of  $\approx 3$  (naked eye visible; e.g., Catchpole et al. 1988; Hamuy et al. 1988). Its evolution has been accurately monitored in different wavelength bands since the outburst, from infrared (e.g., with *Spitzer*, Dwek et al. 2010), to

optical (e.g., with *Hubble Space Telescope (HST)*, Lawrence et al. 2000; Larsson et al. 2011), to X-ray bands (e.g., with *Rosat*, Haberl et al. 2006; *Chandra*, Helder et al. 2013; and *XMM-Newton*, Haberl et al. 2006). This has provided a wealth of high-quality data with unprecedented completeness, making SN 1987A an ideal template to study the SN-SNR connection.

The study, however, is complicated by the interaction of the blast wave with the surrounding inhomogeneous medium. Optical images soon after the outburst revealed an enigmatic triple-ring nebula around the SN (Crofts et al. 1989). The nebula consists mainly of a dense central equatorial ring and two outer rings displaced by about 0.4 pc above and below the central ring and lying in planes almost parallel to the equatorial one. It has been suggested that the nebula might be the result of either the merging of two massive stars that occurred some 20,000 years before the explosion (Morris & Podsiadlowski 2007) or mass loss from a fast-rotating star (Chita et al. 2008).

The interaction of the SN with the nebula is best observed in the radio and X-ray bands. It started about three years after the explosion when both radio and X-ray fluxes began to increase with time (Hasinger et al. 1996; Gaensler et al. 1997). This was interpreted as being due to outer ejecta lighting up the dense wind emitted during a previous red supergiant (RSG) phase and subsequently swept-up by the fast wind during a phase of blue supergiant (BSG) (Chevalier & Dwarkadas 1995). After about 16 years, the soft X-ray lightcurve suddenly steepened still further, contrary to the hard X-ray and radio lightcurves (Park et al. 2005). This was interpreted as being due to the blast wave

sweeping up the dense central equatorial ring (McCray 2007). Since then the soft X-ray flux continued to grow, indicating that the shock is currently still traveling through the dense part of the equatorial ring (Helder et al. 2013).

X-ray observations more than others encode information about the physical properties of both the nebula and the stellar ejecta. Decoding these observations, therefore, might open the possibility to reconstruct the nebula and ejecta structures soon after the SN explosion. This requires accurate and detailed numerical models that are able to follow the ejecta evolution from the SN explosion to the SNR phase and to reproduce the emission properties of both the progenitor SN and its remnant.

Current models, however, were usually aimed at describing either the SN evolution (e.g., Pumo & Zampieri 2011; Handy et al. 2014) or the expansion of the remnant (e.g., Zhekov et al. 2009; Dewey et al. 2012; Potter et al. 2014). The former models describe the early SN evolution and ignore its subsequent interaction with the nebula; the latter assume an initial parametrized ejecta profile that is not proven to reproduce the main observables of the progenitor SN, thus leaving out an accurate description of the ejecta distribution of mass and energy soon after the SN explosion. These limits make it difficult to disentangle the effects of the initial conditions (i.e., the SN event) from those of the boundary conditions (i.e., the interaction with the environment). A first attempt to connect some properties of CC-SN (e.g., the composition and a parameterization of the circumstellar environment) to some observable bulk properties of an SNR has been discussed recently (Patnaude et al. 2015), even though it is by adopting a one-dimensional (1D) approach.

The structure of the pre-SN nebula of SN 1987A is inherently three-dimensional (3D), as is visible in the images from the *HST* (e.g., Larsson et al. 2011). A proper description of the interaction of the ejecta with the nebula therefore requires 3D calculations. To date only a 3D model has been proposed (Potter et al. 2014) to explore the origin of the asymmetric radio morphology observed in SN 1987A. However, this model focuses on the analysis of the radio emission and its initial condition is a parametrized function describing the ejecta distribution about two years after the explosion. As a consequence, the model cannot describe the evolution of the SN and the adopted distribution of ejecta is not proven to be consistent with the observables of the SN.

Here we present a hydrodynamic model describing the evolution of SN 1987A from the breakout of the shock wave at the stellar surface until the expansion of its remnant through the nebula surrounding the SN. We ran several high-resolution simulations to reproduce the main observables of the SN (i.e., bolometric lightcurve, evolution of line velocities, and continuum temperature at the photosphere) and the properties of the X-ray emission of the remnant (i.e., lightcurves, spectra, and morphology). Our simulations cover the first 40 years of evolution to make predictions on the future evolution of the remnant in view of the spatially resolved high-resolution spectroscopy capability of the forthcoming X-ray observatory *Athena* (Nandra et al. 2013). The paper is organized as follows. In Section 2 we describe the hydrodynamic model and the numerical setup, in Section 3 we describe the results, and, finally, we draw our conclusions in Section 4.

## 2. PROBLEM DESCRIPTION AND NUMERICAL SETUP

We first modeled the SN by performing 1D simulations of the “early” post-explosion evolution of a CC-SN during the first 250 days (see Section 2.1). Then the output of these simulations was mapped into 3D to provide the initial condition for the ejecta structure of a 3D model describing the further evolution of the SN and the subsequent development of the SNR interacting with the CSM (see Section 2.2).

### 2.1. Modeling the Post-explosion Evolution of the SN

The post-explosion evolution of the SN was modeled using a 1D Lagrangian code that was specifically tailored to simulate the main observables in CC-SNe (namely the bolometric lightcurve and the time evolution of the photospheric velocity and temperature; Pumo & Zampieri 2011) and widely used to model observed events (Dall’Ora et al. 2014; Spiro et al. 2014; Takáts et al. 2014) including the SN 1987A-like ones (Pastorello et al. 2012).

The code solves the equations of relativistic radiation hydrodynamics in spherical symmetry for a self-gravitating matter fluid that interacts with radiation. Its distinctive features are (1) a fully general relativistic treatment; (2) an accurate treatment of radiative transfer at all regimes (from the one in which the ejecta are optically thick up to when they are optically thin); (3) the coupling of the radiation moment equations with the equations of relativistic hydrodynamics during all the post-explosive phases, adopting a fully implicit Lagrangian finite difference scheme; (4) the computation of heating effects due to decays of radioactive isotopes synthesized in the SN explosion; and (5) the computation of the gravitational effects of the central compact object on the evolution of the ejecta.

Thanks to these characteristics, the code is able to compute the evolution of the stellar ejecta and emitted luminosity from the breakout of the shock wave at the stellar surface up to the so-called nebular stage (i.e., when the envelope has recombined and the energy budget is dominated by the radioactive decays of the heavy elements synthesized in the explosion, see also Section 3.1). At the same time, the code is able to accurately determine the fallback of material on the central object and, as a consequence, the amount of  $^{56}\text{Ni}$  present in the ejected envelope at late times.

The simulations start from the breakout of the shock wave at the stellar surface, using initial conditions that mimic the physical properties of the ejected material after the shock passage following the CC (Pumo & Zampieri 2011). As a consequence, the models depend on some basic parameters that characterize the main radiative, thermal, and dynamical properties of such material. These parameters are the progenitor radius  $R_0$ , the total ejecta energy  $E_{\text{SN}}$ , the envelope mass at shock breakout  $M_{\text{env}}$ , and the total amount of  $^{56}\text{Ni}$  initially present in the ejected envelope  $M_{\text{Ni}}$ . In our simulations  $M_{\text{env}}$  coincides with the total mass surrounding the central compact object at the start of the simulations. This means that during the post-explosive evolution,  $M_{\text{env}}$  is equal to the ejected mass  $M_{\text{ej}}$  plus the mass fallen back to the central compact object. In our models of SN 1987A, the latter mass is of the order of a few hundredths of a solar mass and, as a consequence,  $M_{\text{env}}$  essentially corresponds to  $M_{\text{ej}}$ .

We performed several simulations of the SN evolution, exploring the parameter space defined by  $M_{\text{env}}$  and  $E_{\text{SN}}$ . The

exploration has been restricted to the ranges of values commonly discussed in the literature for SN 1987A (Arnett 1987; Woosley 1988; Utrobin & Chugai 2005; Pumo & Zampieri 2011; Handy et al. 2014): we considered models with  $M_{\text{env}}$  ranging between 8 and 19  $M_{\odot}$  (including the bulk of ejecta and the high-velocity shell), and  $E_{\text{SN}}$  ranging between 1 and  $2 \times 10^{51}$  erg. Also, in our model, the outermost high-velocity shell ( $4000 < v < 20,000 \text{ km s}^{-1}$ ; Lawrence et al. 2000) can be described by a power law with index  $\alpha$  (Shigeyama & Nomoto 1990; Blinnikov et al. 2000). Here we explored models with  $\alpha$  ranging between  $-8$  and  $-9$ , according to the values suggested in the literature (e.g., Woosley 1988). We fixed all the other parameters of the model, namely the initial radius  $R_0 = 3 \times 10^{12}$  cm (which is a reliable value for the progenitor of SN 1987A; Arnett 1996; Young 2004; Pumo & Zampieri 2011) and the initial amount of  $^{56}\text{Ni}$   $M_{\text{Ni}} = 0.07 M_{\odot}$  (corresponding to the amount of Ni synthesized during the explosion of SN 1987A; Arnett et al. 1989).

Note that our 1D SN model cannot simulate possible asymmetries developed during the explosion as suggested by a significant body of observational and simulation evidence. It goes without saying that the most desirable way to model a CC-SN would include a multi-dimensional hydrodynamical calculation that followed the CC, the bounce at nuclear densities, the leakage of neutrinos from the proto-neutron star, the neutrino heating, and the delayed explosion with the shock propagating through the envelope to be ejected. However, current multi-dimensional models can follow the evolution of the exploding star only for a very short time (of the order of few minutes),<sup>5</sup> preventing any possibility of using their output for post-explosion calculations that follow the evolution of the CC-SN ejecta in detail. Conversely, our 1D model allows us to follow the post-explosion evolution of the SN for days, to describe in detail the fallback by using a full-relativistic approach and, therefore, to estimate accurately the total mass ejected in the SN explosion. In addition, our lagrangian code is not flux-limited (as the multi-dimensional codes are), allowing us to accurately simulate the evolution of the ejected material during both the initial phase of the shock breakout and the following nebular phase in which the ejected SN envelope has recombined.

## 2.2. Modeling the SNR Evolution

Optical images clearly show that the structure of the nebula as well as the morphology and evolution of the ejecta are inherently 3D (Kjær et al. 2010; Larsson et al. 2011, 2013). Therefore, once the early phase of the SN explosion was modeled in 1D (see Section 2.1), the output of the SN simulation was mapped into 3D. Then the subsequent evolution and transition from the SN phase to the SNR phase were modeled by numerically solving the time-dependent fluid equations of mass, momentum, and energy conservation; the equations in a 3D Cartesian coordinate system  $(x, y, z)$  take into

account the radiative losses from an optically thin plasma:

$$\begin{aligned} \frac{\partial \rho}{\partial t} + \nabla \cdot \rho \mathbf{u} &= 0, \\ \frac{\partial \rho \mathbf{u}}{\partial t} + \nabla \cdot \rho \mathbf{u} \mathbf{u} + \nabla P &= 0, \\ \frac{\partial \rho E}{\partial t} + \nabla \cdot (\rho E + P) \mathbf{u} &= -n_e n_{\text{H}} \Lambda(T), \end{aligned} \quad (1)$$

where  $E = \epsilon + |\mathbf{u}|^2/2$  is the total gas energy (internal energy,  $\epsilon$ , and kinetic energy),  $t$  is the time,  $\rho = \mu m_{\text{H}} n_{\text{H}}$  is the mass density,  $\mu = 1.3$  is the mean atomic mass (assuming cosmic abundances),  $m_{\text{H}}$  is the mass of the hydrogen atom,  $n_{\text{H}}$  is the hydrogen number density,  $n_e$  is the electron number density,  $\mathbf{u}$  is the gas velocity,  $T$  is the temperature, and  $\Lambda(T)$  represents the radiative losses per unit emission measure. We used the ideal gas law,  $P = (\gamma - 1)\rho\epsilon$ , where  $\gamma = 5/3$  is the adiabatic index.

The calculations were performed using the FLASH code (Fryxell et al. 2000). The hydrodynamic equations were solved using the FLASH implementation of the Piecewise Parabolic Method algorithm (Colella & Woodward 1984). For the present application, the code was extended by additional computational modules to handle the radiative losses  $\Lambda$  (through a table lookup/interpolation method), as well as to calculate the deviations from temperature-equilibration between electrons and ions and the deviations from equilibrium of ionization of the most abundant ions. The output of the latter modules was used in the synthesis of X-ray emission (see Section 2.3).

The 3D simulations started once the majority of the energy released in the explosion was kinetic ( $\sim 26$  hr after the explosion). Note that, at variance with our 1D SN model, the 3D simulations do not include a heating term due to decays of radioactive isotopes synthesized in the SN explosion, such as  $^{56}\text{Co}$  or  $^{44}\text{Ti}$ . On the other hand, in Appendix A, we show that our simplification does not significantly affect the radial profiles of the density and velocity of the ejecta at later times. This evidence supports our assumption to neglect the effect of radioactive heating during the interaction of the remnant with the H II region and with the dense equatorial ring.

We followed the interaction of the blast wave and ejecta with the circumstellar nebula during the first 40 years of evolution (namely until the presumed launch date of the *Athena* X-ray observatory; Nandra et al. 2013). The initial remnant radius was  $\approx 20$  AU ( $\approx 10^{-4}$  pc). As suggested by previous studies (Orlando et al. 2012), we assumed that the initial density structure of the ejecta was clumpy. To this end, after the 1D radial density distribution of ejecta was mapped into 3D, we modeled the ejecta clumps as per-cell random density perturbations derived from a power-law probability distribution (Orlando et al. 2012). The latter distribution, with index  $\xi = -1$ , is characterized by a parameter  $\nu_{\text{max}}$  representing the maximum density perturbation allowed in the simulation. For the purposes of this paper, we assumed that the ejecta clumps have an initial size  $6 \times 10^{12}$  cm (0.4 AU, corresponding to 2% of the initial remnant radius) and a maximum density perturbation  $\nu_{\text{max}} = 5$ . The size and density contrast of the modeled ejecta clumps are in agreement with those suggested by spectropolarimetric studies of SNe (Wang et al. 2003, 2004; Hole et al. 2010).

Initially the blast wave from the SN explosion propagates through the wind of the progenitor BSG. We adopted wind values discussed in the literature (Morris &

<sup>5</sup> However, note that a new approach to follow the post-explosion evolution of the SN in multi-dimensions for a longer time has been proposed recently by Jøgerst et al. (2009).

**Table 1**  
Adopted Parameters of the CSM for the Hydrodynamic  
Models of the SN 1987A Event

CSM Component	Parameters	Units	Range of Values Explored	Best-fit Values
BSG wind:	$\dot{M}_w$	$(M_\odot \text{ year}^{-1})$	$10^{-7}$	$10^{-7}$
	$v_w$	$(\text{km s}^{-1})$	500	500
	$r_w$	(pc)	0.05	0.05
H II region:	$n_{\text{H II}}$	$(10^2 \text{ cm}^{-3})$	[0.8–3]	0.9
	$r_{\text{H II}}$	(pc)	[0.08–0.2]	0.08
Equatorial ring:	$n_{\text{rg}}$	$(10^3 \text{ cm}^{-3})$	[1–2]	1
	$r_{\text{rg}}$	(pc)	0.18	0.18
	$w_{\text{rg}}$	$(10^{17} \text{ cm})$	[0.7–2]	1.7
	$h_{\text{rg}}$	$(10^{16} \text{ cm})$	3.5	3.5
	$\langle n_{\text{cl}} \rangle$	$(10^4 \text{ cm}^{-3})$	[1–3]	$2.5 \pm 0.3$
Clumps:	$\langle r_{\text{cl}} \rangle$	(pc)	[0.14–0.17]	0.155 $\pm 0.015$
	$w_{\text{cl}}$	$(10^{16} \text{ cm})$	[1–3]	1.7
	$N_{\text{cl}}$		[40–70]	50

Podsiadlowski 2007); in particular, we assumed a spherically symmetric wind with a mass-loss rate of  $\dot{M}_w = 10^{-7} M_\odot \text{ yr}^{-1}$  and wind velocity  $v_w = 500 \text{ km s}^{-1}$ ; the wind gas density is proportional to  $r^{-2}$  (where  $r$  is the radial distance from SN 1987A) and the termination shock of the wind is located approximately at  $r_w = 0.05 \text{ pc}$ . Table 1 summarizes the parameters adopted.

The circumstellar nebula probably originates from the interaction of a slow wind from an early RSG phase with a faster wind from a subsequent BSG phase (Kwok et al. 1978). Thus the nebula was modeled assuming that it is composed of a dense inhomogeneous equatorial ring surrounded by an ionized H II region (Chevalier & Dwarkadas 1995; Sugerman et al. 2005). Figure 1 shows an example of the initial configuration of the nebula. The ring (marked red in the figure) consists of a uniform smooth component and high-density spherical clumps mostly located in its inner portion. The smooth component has an elliptical cross section with the major axis  $w_{\text{rg}}$  lying on the equatorial plane. The clumps mimic the protrusions emanating from the equatorial ring and probably formed by hydrodynamic instabilities caused by the interaction of a BSG and an RSG wind (Sugerman et al. 2005). The clumps have all the same diameter  $w_{\text{cl}}$  but their plasma density and radial distance from SN 1987A are randomly distributed around the values  $\langle n_{\text{cl}} \rangle$  and  $\langle r_{\text{cl}} \rangle$ , respectively. The 3D shape and geometry of the H II region were assumed to be analogous to those suggested from the analysis of *HST* data of the ring nebula around the BSG SBW1, which is a candidate twin of the SN 1987A progenitor (Smith et al. 2013).

We explored the parameter space defined by (a) the plasma density  $n_{\text{H II}}$  and inner edge  $r_{\text{H II}}$  of the H II region; (b) the density  $n_{\text{rg}}$ , radial distance from SN 1987A  $r_{\text{rg}}$ , radial extension  $w_{\text{rg}}$ , and height  $h_{\text{rg}}$  of the uniform component of the ring; and (c) the average density  $\langle n_{\text{cl}} \rangle$ , average radial distance from SN 1987A  $\langle r_{\text{cl}} \rangle$ , diameter  $w_{\text{cl}}$ , and number  $N_{\text{cl}}$  of high-density spherical clumps of the ring. In order to limit as much as possible our exploration (which is very computer demanding in the case of a 3D model), we adopted as fiducial values those reported in the literature and found by comparing the results of a 1D hydrodynamic model of SN 1987A with observations

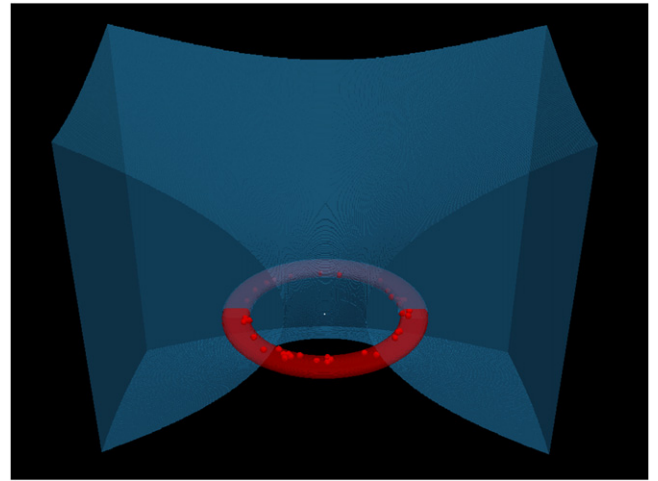


**Figure 1.** Rendition in log scale of the circumstellar nebula around SN 1987A model initial conditions. The ring consists of a uniform smooth component and high-density spherical clumps, and is shown in red; the H II region around the ring is marked by the blue clipped component. The white dot at the center of the coordinate system shows the position of the SN explosion.

(Dewey et al. 2012). Then we explored the parameter space around these values, adopting an iterative process of trial and error to converge on model parameters that reproduce the X-ray lightcurve and spectra of SN 1987A. Table 1 summarizes the ranges of values explored and the parameters of the model best reproducing the data.

We traced the evolution of the different plasma components (namely the ejecta, the H II region, and the ring material) by considering passive tracers associated with each of them. Each material is initialized with  $C_i = 1$ ; whereas,  $C_i = 0$  elsewhere, where the index “i” refers to the ejecta (ej), the H II region (H II), and the ring material (rg). During the remnant evolution, the different materials mix together, leading to regions with  $0 < C_i < 1$ . At any time  $t$ , the density of a specific material in a fluid cell is given by  $\rho_i = \rho C_i$ .

We assumed the SN explosion at the origin of the 3D Cartesian coordinate system  $(x_0, y_0, z_0) = (0, 0, 0)$ . The system is oriented in such a way that the dense equatorial ring lies on the  $(x, y)$  plane. The computational domain extends 1 pc in the  $x$ ,  $y$ , and  $z$  directions. A major challenge in modeling the explosion and subsequent evolution of SN 1987A was the very small scale of the system in the immediate aftermath of the SN explosion (the initial remnant radius is  $\approx 10^{-4} \text{ pc}$ ) with the size of the rapidly expanding blast wave. To capture this range of scales, we exploited the adaptive mesh refinement capabilities of the FLASH code, by employing 18 nested levels of refinement with resolution increasing twice at each refinement level. The refinement/derefinement criterion (Löhner 1987) implemented in FLASH follows the changes in mass density, temperature, tracer of ejecta, and tracer of the ring.

The calculations were also performed using an automatic mesh derefinement scheme in the whole spatial domain that kept the computational cost approximately constant as the blast expanded (Orlando et al. 2012): the maximum number of refinement levels used in the calculation gradually decreased from 18 (initially) to 9 (at the final time), following the expansion of the blast and ensuring a number of grid zones per radius of the remnant  $> 100$  during the whole evolution. At the beginning (at the end) of the simulation, this grid configuration yielded an effective resolution of  $\approx 10^{-6} \text{ pc}$  ( $\approx 5 \times 10^{-4} \text{ pc}$ ) at

the finest level, corresponding to  $\approx 100$  zones per initial radius of the remnant ( $>600$  zones per final radius of the remnant). The effective mesh size varied from  $(10^6)^3$  initially to  $2048^3$  at the final time. Note that the maximum spatial resolution achieved by Potter et al. (2014) in their 3D model was  $\approx 4 \times 10^{-3}$  pc (corresponding to an effective mesh size of  $256^3$ ) during the whole evolution.

The high spatial resolution achieved in our simulations required about 7 millions of CPU hours on the MareNostrum III cluster hosted at the Barcelona Supercomputing Center (Barcelona, Spain) and about 4 millions of CPU hours on the FERMI cluster hosted at CINECA (Bologna, Italy). Most of these resources were made available by a large computational program awarded in the framework of the PRACE (Partnership for Advanced Computing in Europe) initiative to enable high-impact scientific research with a pan-European supercomputing infrastructure,<sup>6</sup> which is the top level of the European high performance computing systems.

### 2.3. Synthesis of X-Ray Emission

From the model results, we synthesized the X-ray emission originating from the interaction of the blast wave with the surrounding nebula, following an approach analogous to that of previous studies (Orlando et al. 2006, 2009). The results of the numerical simulations are the evolution of temperature, density, and velocity of the plasma in the whole spatial domain. We rotated the system about the three axes to fit the inclination of the ring as found from the analysis of optical data (Sugerman et al. 2005), namely  $i_x = 41^\circ$ ,  $i_y = -8^\circ$ , and  $i_z = -9^\circ$ .

In the case of fast collisionless shocks, such as those observed in SNRs, the synthesis of X-ray emission has to take into account the lack of temperature-equilibration between electrons and ions. In fact, the jump conditions at shock speeds exceeding  $500 \text{ km s}^{-1}$  drive thermal and dynamic changes of the plasma on very short timescales. Most of the shock energy is transferred to ions (Ghavamian et al. 2007), so that the ratio of the electron to ion temperature  $\beta$  in the post-shock region is generally less than 1: the larger the shock velocity, the smaller the  $\beta$ . We computed this effect in our model by considering that the equilibration in the post-shock plasma is reached through Coulomb collisions, which are expected to proceed relatively slowly (Ghavamian et al. 2007), leading to  $\beta < 1$ . To take this effect into account, we added an additional passive tracer to the model equations that stores the time  $t_{\text{shj}}$  when the plasma in the  $j$ th domain cell was shocked. Then the electron temperature in each cell was calculated from the time  $t_{\text{shj}}$  and from the ion temperature and plasma density derived by integrating Equations (1). More specifically, we assumed that the electrons are heated almost instantaneously at the shock front up to  $kT \sim 0.3 \text{ keV}$  (regardless of the shock Mach number) by lower hybrid waves (Ghavamian et al. 2007), as suggested for shock velocities of the order of  $10^3 \text{ km s}^{-1}$  like those in our simulations. Then we calculated the evolution of ion and electron temperatures in each cell of the post-shock medium by including the effects of the Coulomb collisions. This evolution was calculated in the time  $\Delta t_j = t - t_{\text{shj}}$  ( $t$  is the current time) since the plasma in the cell was shocked.

Another important effect to take into account in the synthesis of X-ray emission from fast shocks is the time lag of the plasma to change its ionization from a cool to a hot state. If the

**Table 2**  
Adopted Parameters in the Synthesis of X-Ray Emission

Parameter	Value <sup>a</sup>	Reference
$D$	51.4 kpc	Panagia (1999)
$N_{\text{H}}$	$2.35 \times 10^{21} \text{ cm}^{-2}$	Park et al. (2006)
He	2.57	Zhekov et al. (2009)
C	0.03	Zhekov et al. (2009)
N	0.56	Zhekov et al. (2009)
O	0.081	Zhekov et al. (2009)
Ne	0.29	Zhekov et al. (2009)
Mg	0.28	Zhekov et al. (2009)
Si	0.33	Zhekov et al. (2009)
S	0.30	Zhekov et al. (2009)
Ar	0.537	Zhekov et al. (2009)
Ca	0.03	Zhekov et al. (2009)
Fe	0.19	Zhekov et al. (2009)
Ni	0.07	Zhekov et al. (2009)

**Note.**

<sup>a</sup> The abundances are relative to the solar photospheric values (Anders & Grevesse 1989).

timescale of the temperature increase at the shock front is much shorter than the ionization and recombination timescales, the plasma ions can be at a lower ionization state than the equilibrium state corresponding to the local electron temperature (Hamilton et al. 1983). Such deviations from equilibrium of ionization may have dramatic effects on the interpretation of observations. They are taken into account in our model by following an approach discussed in the literature (Dwarkadas et al. 2010), which is particularly effective in the case of 3D simulations in order to have high efficiency together with a reasonable accuracy in the synthesis of X-ray emission. From the values of emission measure, electron temperature, and maximum ionization age in the  $j$ th domain cell, the corresponding X-ray spectrum is synthesized by using the non-equilibrium of ionization (NEI) emission model VPSHOCK available in the XSPEC package along with the ‘‘NEI version 2.0’’ atomic data from ATOMDB (Smith et al. 2001). The emission measure in the  $j$ th domain cell is  $\text{em}_j = n_{\text{ej}}^2 V_j$  (where  $n_{\text{ej}}$  is the particle density in the cell and  $V_j$  is the cell volume); the electron temperature in the cell  $T_{\text{ej}}$  is computed by taking into account the deviations from temperature-equilibration as described above; and the maximum ionization age in the cell is  $\tau_j = n_{\text{ej}} \Delta t_j$  (where  $\Delta t_j$  is the time since the plasma in the cell was shocked; see above).

We assumed the source at a distance  $D = 51.4 \text{ kpc}$  (Panagia 1999). We adopted the metal abundances derived from the analysis of deep *Chandra*/LETG and HETG observations of SN 1987A (Zhekov et al. 2009) and summarized them in Table 2. The X-ray spectrum from each cell was filtered through the photoelectric absorption by the ISM, assuming a column density  $N_{\text{H}} = 2.35 \times 10^{21} \text{ cm}^{-2}$  (Park et al. 2006). We integrated the absorbed X-ray spectra from the cells in the whole spatial domain. The spectra were then folded through the instrumental response of the X-ray instruments of interest, obtaining the relevant focal-plane spectra. In such a way, we derived X-ray spectra as they would be collected with *XMM-Newton*/EPIC and, in the near future, with *Athena*/WFI and X-ray images as they would be collected with *Chandra*/ACIS. The synthesized spectra and images were put in a format identical to that of real X-ray observations and analyzed with

<sup>6</sup> <http://www.prace-ri.eu>

the standard data analysis system used for the specific instruments of interest.

### 3. RESULTS

#### 3.1. Post-explosion Evolution of the SN

The post-explosion evolution of the simulated SN 1987A follows the trend described in detail by Pumo & Zampieri (2011). Here we summarize the main phases. The evolution is guided by the thermodynamics of the expanding ejecta and passes through three different phases. Initially, the envelope is completely ionized and optically thick, and the emission is due to the release of internal energy on a diffusion timescale (diffusive phase). Then the ejecta recombine and the emission is dominated by the sudden release of energy caused by the receding motion of the wavefront through the envelope (recombination phase). Finally, the envelope is recombined and optically thin to optical photons, and the emission comes from the thermalization of the energy deposited by gamma-ray photons (radioactive-decay phase or nebular phase). Usually the first two phases are globally referred as the photospheric phase, during which it is possible to compare the observed photospheric temperature and velocity with the corresponding simulated quantities, which is contrary to the nebular phase where the same notion of photosphere loses its meaning (Bersten et al. 2011; Pumo & Zampieri 2011). We adopted the so-called inflection time  $t_{\text{inf}}$  (measured from the explosion epoch) as a measurement of the duration of the photospheric phase (Pumo & Zampieri 2013); for SN 1987A  $t_{\text{inf}} \approx 100$  days.

From the models, we derived the main observables (namely the bolometric lightcurve and the evolution of the photospheric temperature and velocity) during the first 250 days after the explosion. Then we compared the model results with observations of SN 1987A by performing a simultaneous  $\chi^2$  fit of these observables, thus constraining the ejected mass and the explosion energy of the SN. We found the comparison with the observations satisfactory for models with a total energy ranging between 1.2 and  $1.4 \times 10^{51}$  erg and an envelope mass between 15 and  $17 M_{\odot}$  (see Figure 2). Figure 3 shows the radial distribution of mass density 26 hr after the breakout of the shock wave at the stellar surface for the models best reproducing the observations (see Table 3 for details). Note that runs SN-M17-E1.2-N8 and SN-M17-E1.2-N9 differ only for the slope of the power law describing the high-velocity shell of the SN (see Section 3.1): the density and kinetic energy in the outer envelope are lower for the steeper profile of density. The ejecta distribution in this outer shell does not change the observables of the SN significantly.

The difficulty of reproducing the observables at early time in Figure 2 is mainly due to the initial conditions used in our simulations (see Section 2.1), while some less prominent discrepancies at late times (80–110 days) might be explained by the absence of nonthermal ionization from gamma rays in our model (Pumo & Zampieri 2011).

The comparison of model results with observations enabled us to constrain the bulk of envelope mass  $M_{\text{env}}$  and the energy of the explosion  $E_{\text{SN}}$ . On the other hand, no firm conclusions on the distribution of energy and mass in the high-velocity shell of the SN were obtained from the analysis of SN observables.

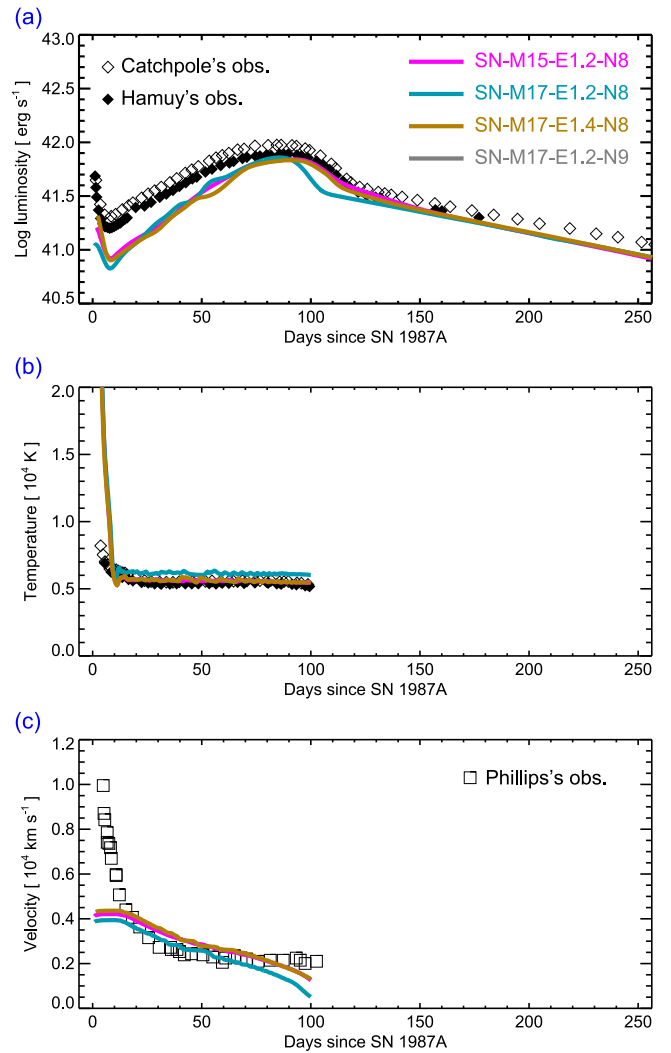


**Figure 2.** Bolometric lightcurves (a) and evolution of the photospheric temperature (b) and velocity (c) derived from the models listed in Table 3 (solid colored lines), compared to the corresponding quantities of SN 1987A (Catchpole et al. 1987, 1988; Hamuy et al. 1988; Phillips et al. 1988; empty squares and filled and empty diamonds). The photospheric temperature and velocity can be defined from the model during the so-called photospheric phase (see text), corresponding to the first  $\sim 100$  days of evolution. Models SN-M17-E1.2-N8 and SN-M17-E1.2-N9 overlap each other.

#### 3.2. Remnant Expansion through the Circumstellar Nebula

We followed the evolution from the SN phase to the SNR phase for 40 years, restricting our analysis to SN models reproducing the main observables of SN 1987A during the first 250 days of evolution (listed in Table 3). Then, we explored the space of parameters describing the CSM (mainly the equatorial ring and the H II region) and compared the X-ray lightcurves and spectra synthesized from the models with those observed in SN 1987A (see Figure 5).

In all the cases investigated, the evolution follows the same general trend. Initially, the blast wave from the SN propagates through the wind of the progenitor BSG. About three years after explosion, the ejecta reach the H II region (see online movie) and the transition from SN to SNR enters into the first phase of evolution (H II-region-dominated phase). Forward and reverse shocks are generated; the former propagates into the H II region and the latter is driven back into the ejecta (see Figure 4). The X-ray emission begins to increase rapidly with

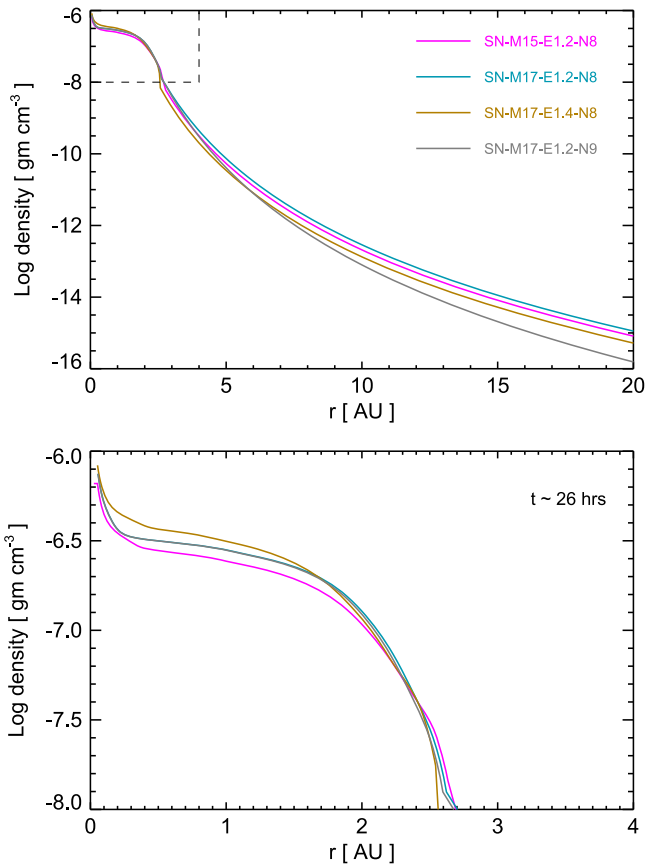


**Figure 3.** (Top) Radial density profiles of ejecta for the models reproducing the main observables of SN 1987A (see Table 3 and Figure 2) at  $t \sim 26$  hr after the shock breakout. Different colors mark different models. (Bottom) Enlargement of the region marked with a box in the top panel, showing the details of the bulk of the ejecta.

**Table 3**

Parameters of the SN Models Reproducing the Main Observables of SN 1987A During the First 250 Days from the Outburst

Model	$M_{\text{env}}$ ( $M_{\odot}$ )	$E_{\text{SN}}$ ( $10^{51}$ erg)	$\alpha$	$R_0$ ( $10^{12}$ cm)	$M_{\text{Ni}}$ ( $M_{\odot}$ )
SN-M17-E1.2-N8	17	1.2	-8	3	0.07
SN-M15-E1.2-N8	15	1.2	-8	3	0.07
SN-M17-E1.4-N8	17	1.4	-8	3	0.07
SN-M17-E1.2-N9	17	1.2	-9	3	0.07

time and is dominated by emission from the shocked plasma of the H II region and by a smaller contribution of shocked ejecta in the outer SN envelope. This is evident from the lightcurves (Figure 5), the spectra (Figure 6), and the emission morphology (Figure 8 and online movie). The emitting plasma is largely out of equilibrium of ionization and its emission measure distribution as a function of electron temperature,  $kT_e$ , and ionization timescale,  $\tau$ , peaks at  $kT_e \approx 2$  keV and  $\tau \approx 3 \times 10^{10} \text{ s cm}^{-3}$  with a sharp distribution that can be approximated with an isothermal plasma component (see upper panels of Figure 7). This is in excellent agreement with the best-fit parameters derived from the spectral fitting with the isothermal components of X-ray spectra of SN 1987A at this epoch (see Appendix B). This phase lasts until the blast wave hits the equatorial ring (year 15).

In the H II-region-dominated phase, we found that the sudden increase observed in the soft X-ray band ([0.5, 2] keV) is best-fitted by models in which the outer layers of ejecta have a post-explosion radial profile of density approximated by a power law with index  $\alpha = -8$  (see Figure 5(b)). On the contrary, we found that models with index  $\alpha = -9$  systematically underestimate the soft X-ray flux during the first seven years, even by changing the values of  $n_{\text{H II}}$  and  $n_{\text{H I}}$  within the range of values compatible with observations. This is evident in Figure 9, where we report the result for the model with  $\alpha = -9$  best approximating the observations: the discrepancy between the model results and observations is evident for  $t < 7$  years, even though the same model fits well the bolometric lightcurve of the SN during the first 250 days of evolution (see Figure 2) and the X-ray lightcurves for  $t > 7$  years (Figure 9). Table 4 reports the parameters of this model to be compared with those of the model with  $\alpha = -8$  shown in Table 1. The reason for this discrepancy is the content of energy and mass of the outer shell of ejecta, which is the first material hitting the nebula and, thus, determining the early X-ray emission from the ejecta-nebula interaction. Models with  $\alpha = -9$  have less mass and energy in the outer shell than models with  $\alpha = -8$  and, as a result, the corresponding soft X-ray lightcurve rises more slowly and fails to fit the observations.

Note that the value of  $\alpha$  has little (if any) effect in determining the main observables of the SN (e.g., the bolometric lightcurve) during the first 250 days of evolution. SN models with the same envelope mass and total energy but with different values of  $\alpha$  lead to very similar results (see Figure 2). This is due to the fact that the observables of the SN depend on the bulk of ejecta. Our findings, therefore, show that the X-ray emission originating from the SNR in this phase can constrain the structure of outermost ejecta better than the emission from the SN. Because the density profile of the ejecta is expected to depend on the structure of the progenitor star and on the shock acceleration of the gas during the explosion, studying the early interaction of the ejecta with the nebula may provide important clues to the latest stage of stellar evolution, and may be used as a probe of the mechanisms involved in the SN engine.

During the H II-region-dominated phase, the model also enabled us to constrain the parameters characterizing the H II-region (namely its density and inner radius); the best-fit parameters are listed in Table 1.

Around year 13 the blast wave hits the first dense clump of the equatorial ring and around year 15 it reaches the inner edge of the ring (see Figure 4 and online movie). The transition from SN to SNR then enters into the second phase of evolution (ring-dominated phase), which lasts until year 32, when the forward shock propagates beyond the majority of the dense ring material. This phase is characterized by the interaction of the forward shock with the dense clumps of the ring. Each shocked clump evolves toward a core-plume structure, with a crescent-like shape characterized by Kelvin-Helmholtz instabilities developing in the downstream region (see Figure 10 and online movie). As the shock travels through the clump, Rayleigh-Taylor instabilities develop on the upstream side of the clump, leading to its progressive fragmentation. A complex pattern of filaments and fragments forms in the interclump region, with densities varying between  $\sim 10^3 \text{ cm}^{-3}$  in the smooth component of the ring and  $\sim 10^4 \text{ cm}^{-3}$  in proximity of the clumps. Note that the appropriate description of the shock-clump interaction required the high spatial resolution adopted in our

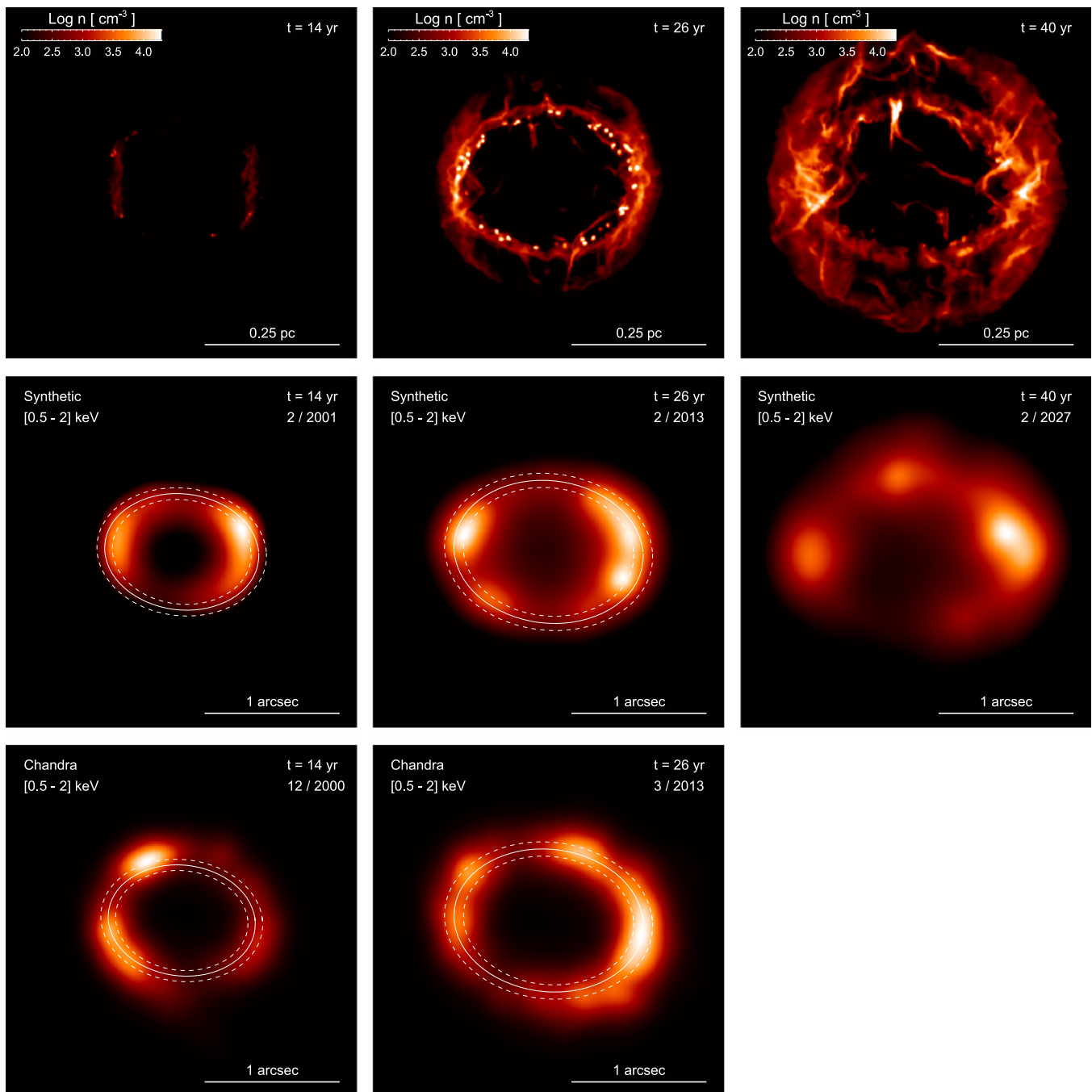


**Figure 4.** Interaction of the blast wave with the nebula. (Top) Three-dimensional volume rendering of the particle density of the shocked plasma at the labeled times. (Middle) Corresponding synthetic maps of X-ray emission in the [0.5, 2] keV band integrated along the line of sight. Each image has been normalized to its maximum for visibility and convolved with a Gaussian of size 0.15 arcsec to approximate the spatial resolution of *Chandra* observations (Helder et al. 2013). (Bottom) Maps of X-ray emission of SN 1987A collected with *Chandra* at the labeled times, and normalized to their maximum for visibility (see Appendix B). The overplotted ellipsoids represent the projection of circles lying in the equatorial plane of SN 1987A and fitting the position of the maximum X-ray emission in each observation. The dashed lines show an uncertainty of 10%.

(An animation of this figure is available.)

simulations. The modeled features cannot be reproduced at lower resolutions (e.g., Potter et al. 2014).

In this phase, the contribution from the shocked ring dominates the X-ray emission (see Figures 5–8 and online movie). The shocked cores of the clumps lead predominantly to soft X-rays and determine the further steepening of the soft X-ray lightcurve (Figure 5(b)). This emitting plasma

component is essentially in collisional ionization equilibrium and its emission measure peaks to electron temperature  $kT_e \approx 0.5$  keV and ionization timescale  $\tau \approx 5 \times 10^{13} \text{ s cm}^{-3}$  (see middle panels of Figure 7). We can roughly identify this material with the plasma component with  $\tau > 10^{13} \text{ s cm}^{-3}$  derived from the spectral fitting of X-ray spectra of SN 1987A collected with current X-ray observatories for  $t > 15$  years

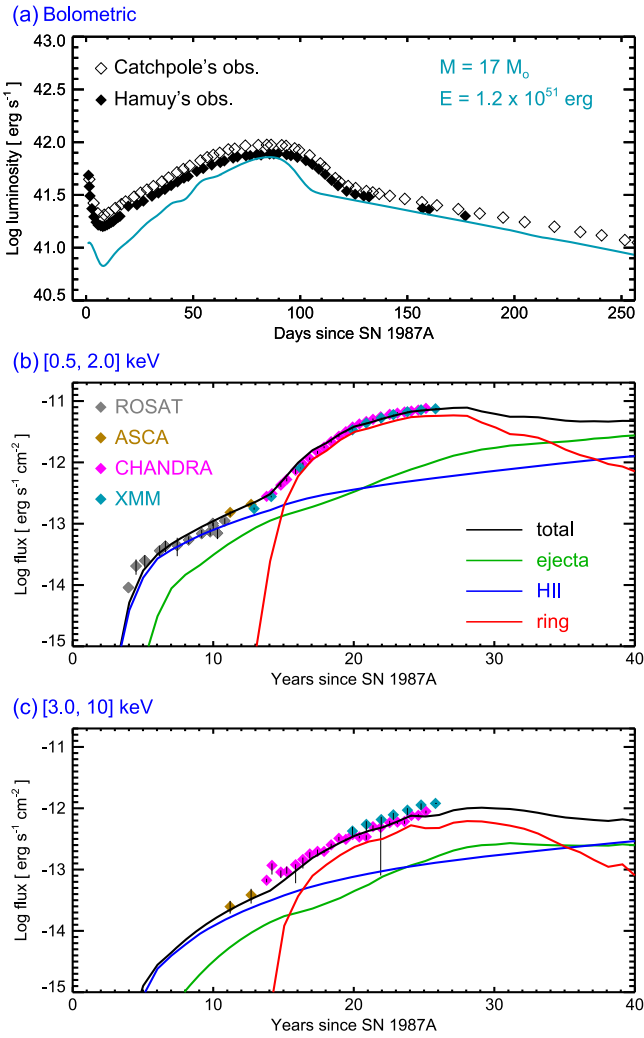


**Figure 5.** Observed and modeled lightcurves. (a) Bolometric lightcurve of our favored model (cyan line) compared to the lightcurve of SN 1987A (filled and empty diamonds; Catchpole et al. 1987, 1988; Hamuy et al. 1988). (b) X-ray lightcurve in the [0.5, 2] keV band synthesized from the favored model (black line) compared to the lightcurve of SN 1987A observed with Rosat (gray diamonds; Haberl et al. 2006), ASCA (brown; see Appendix B), Chandra (magenta; Helder et al. 2013), and XMM-Newton (cyan; Haberl et al. 2006; Maggi et al. 2012; see Appendix B). Green, blue, and red lines mark the contribution to emission from the shocked ejecta, the shocked plasma from the H II region, and the shocked plasma from the ring, respectively. (c) Same as in Figure 5(b) but for the lightcurve in the [3, 10] keV band.

(e.g., Helder et al. 2013; see also Appendix B). The smooth component of the ring and the fragments of the shocked clumps stripped by hydrodynamic instabilities dominate the emission in the hard band. This plasma component causes the broadening of the emission measure distribution around the peak due to shocked clumps, and includes plasma with  $kT_e$  up to  $\sim 2$  keV and  $\tau$  down to  $\sim 10^{11}$  s cm<sup>-3</sup> (see middle panels of Figure 7). In addition, a significant contribution to the emission with  $kT_e > 1$  keV and  $\tau < 10^{11}$  s cm<sup>-3</sup> comes from the shocked ejecta. Given the complexity of the emission measure distribution in this phase, it is not obvious to attribute a physical meaning to the isothermal components with  $\tau < 10^{13}$  s cm<sup>-3</sup> derived from the spectral fitting of the X-ray spectra of SN 1987A and largely used in the literature (see Appendix B). Indeed, the physical origin of the observed X-ray spectra is unveiled by our hydrodynamic model, as shown in

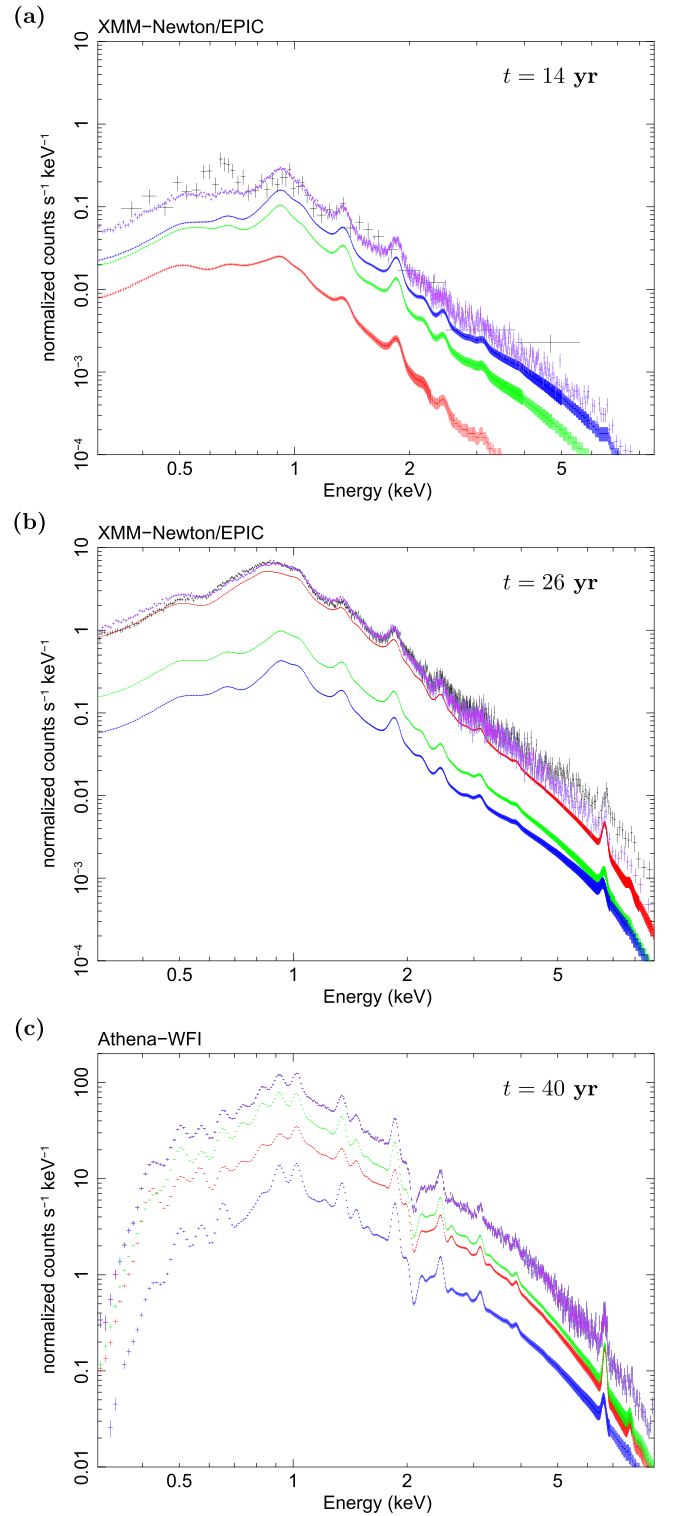


**Figure 6.** Synthetic and observed X-ray spectra of SN 1987A. (a) XMM-Newton/EPIC-pn spectra at  $t = 14$  years. The true spectrum is marked in black (see Appendix B); the synthetic spectrum from the whole shocked plasma is marked in magenta; the contributions to emission from the different shocked plasma components are marked in green (ejecta), red (ring), and blue (H II region). (b) As in Figure 6(a), for  $t = 26$  years. (c) As in Figure 6(a), for  $t = 40$  years and for spectra as they would be collected with Athena/WFI.

Figure 7. From the model best reproducing the X-ray lightcurves and spectra, we were able to constrain the parameters characterizing the equatorial ring (see Table 1 for details).

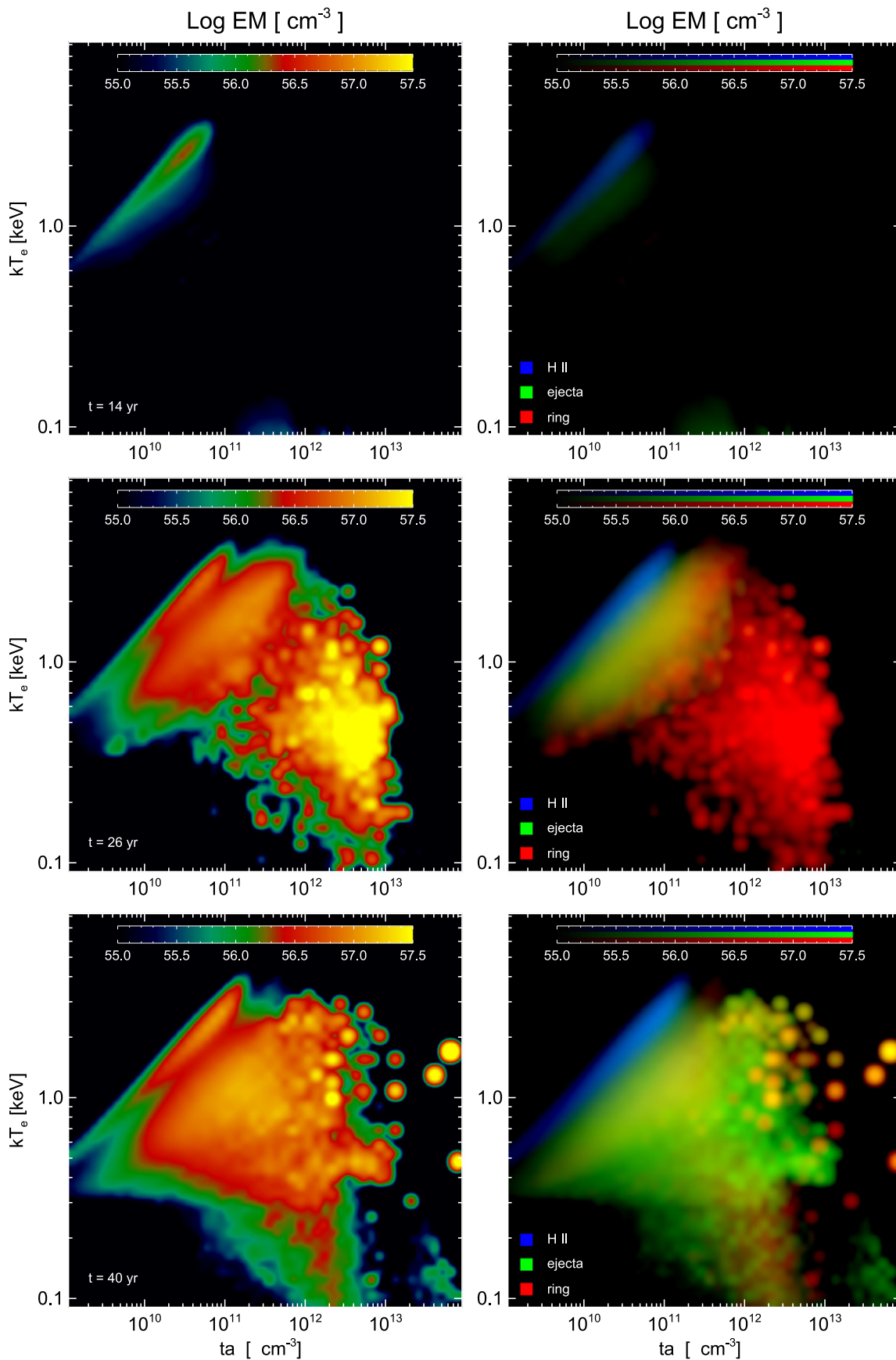


**Figure 7.** Left: distributions of emission measure vs. electron temperature  $kT_e$  and ionization timescale  $\tau$  at the labeled times, corresponding to the X-ray spectra shown in Figure 6. Right: corresponding three-color composite images of the emission measure distributions. The colors show the contribution to emission measure from the different shocked plasma components, namely the ejecta (green), the ring (red), and the H II region (blue).

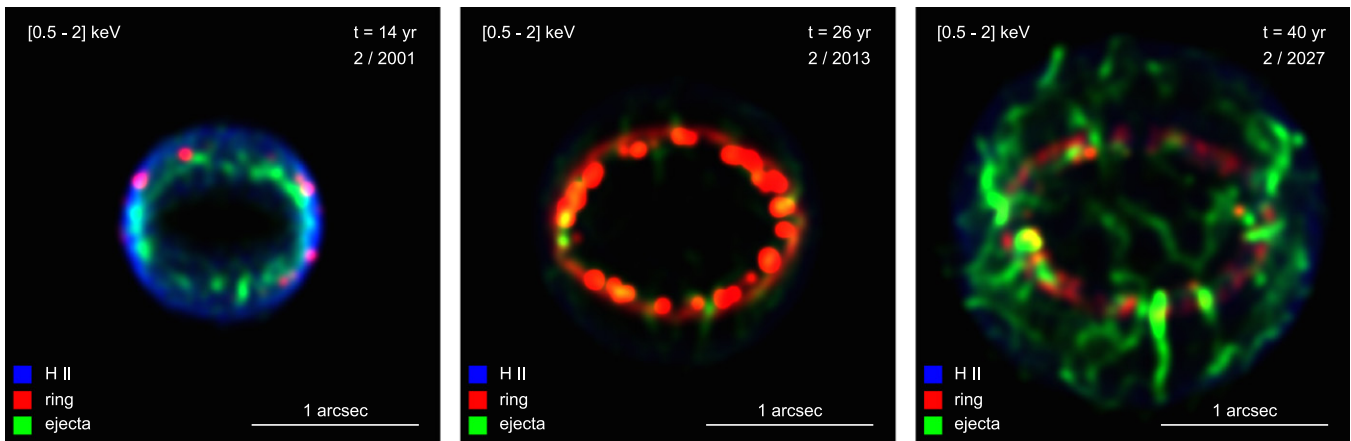


**Figure 8.** Three-color composite images of the X-ray emission in the [0.5, 2] keV band integrated along the line of sight at the labeled times. Each image has been normalized to its maximum for visibility and smoothed with a Gaussian of size 0.025 arcsec. The colors in the composite show the contribution to emission from the different shocked plasma components, namely the ejecta (green), the ring (red), and the H II region (blue).

(An animation of this figure is available.)

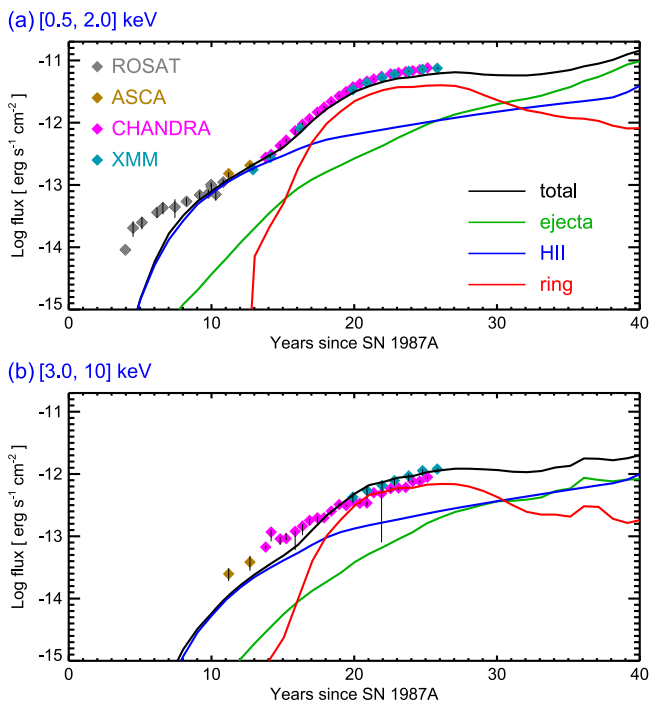


**Figure 9.** As in Figures 5(b) and (c) for a model with envelope mass  $M_{\text{env}} = 17 M_{\odot}$ , ejecta energy  $E_{\text{SN}} = 1.2 \times 10^{51}$  erg, and with the density profile of ejecta in the high-velocity shell approximated by a power law with index  $\alpha = -9$  (run SN-M17-E1.2-N9 in Table 3). The parameters of the CSM of this model are reported in Table 4.

During the first two phases of evolution, the remnant morphology in the X-ray band synthesized from the model appears very similar to that observed. In particular, in the ring-dominated phase, the morphology is characterized by bright knots originating from the shocked clumps and resembles that of SN 1987A (see Figures 4, 8, and online movie). In Figure 4 we compare the synthetic and observed morphology at two different epochs (years 14 and 26). The ellipsoids overlaid in the figure represent the projection of circles lying in the equatorial plane of SN 1987A and fitting the position of the maximum X-ray emission in the observations. Although the extension of the X-ray source synthesized from the model

**Table 4**  
Parameters of the CSM for the Hydrodynamic Model with  $\alpha = -9$   
Best Approximating the X-Ray Lightcurves

CSM Component	Parameters	Units	Best-fit Values
BSG wind:	$\dot{M}_w$	$(M_{\odot} \text{ year}^{-1})$	$10^{-7}$
	$v_w$	$(\text{km s}^{-1})$	500
	$r_w$	(pc)	0.05
H II region:	$n_{\text{H II}}$	$(10^2 \text{ cm}^{-3})$	20
	$r_{\text{H II}}$	(pc)	0.1
Equatorial ring:	$n_{\text{rg}}$	$(10^3 \text{ cm}^{-3})$	1
	$r_{\text{rg}}$	(pc)	0.18
	$w_{\text{rg}}$	$(10^{17} \text{ cm})$	1.7
	$h_{\text{rg}}$	$(10^{16} \text{ cm})$	3.5
	$\langle n_{\text{cl}} \rangle$	$(10^4 \text{ cm}^{-3})$	$1.3 \pm 0.3$
Clumps:	$\langle r_{\text{cl}} \rangle$	(pc)	$0.17 \pm 0.015$
	$w_{\text{cl}}$	$(10^{16} \text{ cm})$	1.7
	$N_{\text{cl}}$		40

seems to be smaller than the observed one (suggesting a modeled blast wave slightly slower than observed), the synthetic maps fit those observed within an uncertainty of 10% (dashed lines). In particular, at year 14, the observations show a bright knot at north-west that may indicate that the observed blast wave is at a distance larger than that in our model. On the other hand, the knot is also well beyond the ellipsoid fitting the position of the forward shock in the equatorial plane, suggesting that the knot is probably the result of the interaction of the blast wave with some inhomogeneity at some height above the equatorial plane. This feature could be reproduced in our model considering, for instance, an overdense clump located well above the equatorial plane.

The remnant enters into the third phase (ejecta-dominated phase) around year 32, when the contribution of shocked ejecta to the soft X-ray emission becomes the dominant component (see Figures 5–8). The reverse shock travels through the innermost ejecta with higher densities. Now the emitting plasma is characterized by a broad emission measure distribution that peaks at  $kT_e \approx 1$  keV and  $\tau \approx 5 \times 10^{11} \text{ s cm}^{-3}$ ; although it is also characterized by few spikes with  $\tau > 10^{13} \text{ s cm}^{-3}$  due to the interaction of high-density clumps of ejecta with the ring (see lower panels of Figure 7 and right panel in Figure 8). The

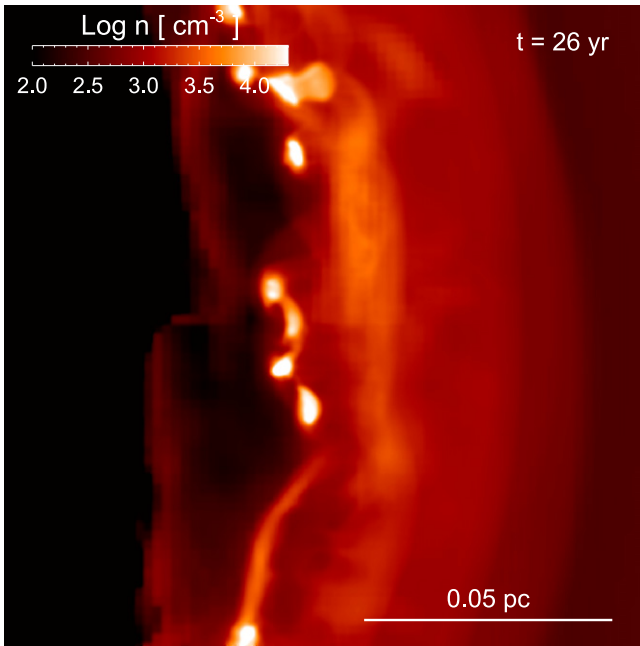


**Figure 10.** Three-dimensional volume rendering of particle density of the shocked plasma at  $t = 26$  years. The line of sight is aligned with the  $z$  axis and the supernova is located to the left of this plot. The figure shows a close-up view of the interaction of the ejecta with the ring in the equatorial plane. The bright knots are shocked clumps of the ring.

(An animation of this figure is available.)

remnant morphology shows a revival of very bright knots, which are now due to shocked clumps of ejecta rather than clumps of the ring (see Figure 4 and online movie). Our simulations show that, in this phase, the evolution of the X-ray emission depends on the density distribution of the outermost ejecta as in the H $\pi$ -region-dominated phase. Models with the same explosion energy and envelope mass but with a different slope of the density profile of ejecta lead to significantly different X-ray lightcurves after year 32 (compare Figures 5 and 9). In particular, we found that the steeper the density profile, the higher the contribution of shocked ejecta to X-ray emission after year 32. In the next future, therefore, SN 1987A will offer the possibility to directly study the structure and chemical composition of the innermost ejecta and the imprint of the metal-rich layers inside the progenitor star.

### 3.3. The Central Compact Remnant

Pioneering studies by Fransson & Chevalier (1987) suggested that the dense shells of expanding ejecta may obscure the X-ray emission of the compact object (if any) of SN 1987A for a few decades. Our model describes the distribution of the ejecta (shocked and unshocked) as well as the complex circumstellar environment. Thus, the model allows us to get a thorough description of the local absorption in the remnant and to derive constraints on the X-ray emission of its yet undetected central source.

The effective surface temperature of an isolated neutron star with an age of 10–30 years is expected to be in the range  $T_{\text{eff}} \sim 3\text{--}6$  MK (e.g., Shternin & Yakovlev 2008). This temperature should stay constant until the age of the star is lower than its thermal relaxation time,  $t_{\text{rel}}$ , which is in the range 30–300 years, depending on the properties of the stellar crust and of its core (e.g., Shternin & Yakovlev 2008). From the

analysis of *Chandra* observations, Ng et al. (2009) derived an upper limit of 0.010 counts per second for the central source (in the [0.08, 10] keV energy band) on the basis of its non-detection in the *Chandra*-HRC data. Without accounting for the local absorption, this upper limit corresponds to a surface temperature lower than  $\approx 2.5$  MK, which is at odds with predictions from standard theories and may suggest extremely short values of  $t_{\text{rel}}$  due, for example, to superfluidity or quark matter.

Our model shows that, at the present epoch, the column density toward the center of the remnant<sup>7</sup> is  $N_{\text{H}} \approx 4.5\text{--}5 \times 10^{22} \text{ cm}^{-2}$ , which is mainly associated with the unshocked ejecta. This local absorbing column density is almost a factor of 20 higher than the interstellar absorption toward the Large Magellanic Cloud and allows us to revise the constraints on the thermal emission from the central source suggested by Ng et al. (2009). By accounting for the local absorption, we then obtained an upper limit of 3.9 MK for the surface temperature (i.e., a bolometric luminosity  $L_{\text{bol}} = 1.6 \times 10^{35} \text{ erg s}^{-1}$ ), by considering a neutron star with radius  $R_{\text{NS}} = 10 \text{ km}$  at a distance of 51.4 kpc. This revised value is in good agreement with standard theories, which suggest bolometric luminosities  $L_{\text{bol}} > 5 \times 10^{34} \text{ erg s}^{-1}$  (e.g. Yakovlev & Pethick 2004) without invoking the presence of very short values of  $t_{\text{rel}}$ .

The X-ray emission from young pulsars is typically dominated by a nonthermal component. Therefore, we also considered the case of nonthermal radiation by assuming a characteristic power-law index  $\Gamma = 1.5$ . Taking into account the high local absorption from the unshocked ejecta, we found that the count-rate upper limit obtained with *Chandra* converts to a luminosity  $L_{\text{nt}} \sim 6 \times 10^{35} \text{ erg s}^{-1}$  in the [2, 10] keV band, corresponding to a flux of  $\sim 0.1$  mCrab at 51.4 kpc (to be compared with  $L_{\text{nt}} \sim 7 \times 10^{34} \text{ erg s}^{-1}$  obtained by Ng et al. 2009).

Finally we studied the variation of the local absorption with time, finding a relatively fast decrease. In particular, we verified that the expansion of the ejecta will reduce the column density by a factor of  $\sim 2$  ( $N_{\text{H}} \approx 2 \times 10^{22} \text{ cm}^{-2}$ ) at the end of our simulation (corresponding to 40 years after the explosion), namely at the presumed launch date of the *Athena* X-ray observatory (Nandra et al. 2013).

It is worth noting that, according to our model, the bulk of the absorption originates in the ejecta. The high metallicity of the expanding ejecta strongly enhances their optical depth with respect to a medium with a solar chemical composition, the O-rich ejecta heavily absorbing the X-ray radiation below 1 keV, and the Si-, S-, and Fe-rich ejecta contributing at higher energies (see Wilms et al. 2000 for details). We can thus consider our estimates (obtained by assuming a solar composition) as conservative. A detailed description of the local absorption, however, would require a detailed knowledge of the distribution of the chemical abundances in the ejecta, which is beyond the scope of this paper.

## 4. SUMMARY AND CONCLUDING REMARKS

We investigated how the morphology and the emission properties of the remnant of SN 1987A reflect (1) the physical characteristics of the progenitor SN and (2) the early interaction

<sup>7</sup> We inspected a region  $\approx 3 \times 10^{17} \text{ cm}$  wide (corresponding to  $\approx 0.2$  arcsec considering the distance of  $\approx 51.4$  pc) to account for a possible proper motion of the central object around the geometrical center of the remnant, finding limited variations of the absorbing column.

of the SN blast wave with the surrounding inhomogeneous nebula. To this end, we developed a model describing SN 1987A from the breakout of the shock wave at the stellar surface up to the 3D expansion of its remnant. A major challenge was capturing the enormous range in spatial scales (spanning six orders of magnitude) that required a very high spatial resolution (down to  $\sim 0.2$  AU). We performed an exploration of the parameter space, searching for a model simultaneously reproducing both the observables of the SN (i.e., bolometric lightcurve, evolution of line velocities, and continuum temperature at the photosphere) and the X-ray emission of the remnant (i.e., lightcurves, spectra, and morphology). Our findings lead to several conclusions:

1. We identified three phases in the evolution (see Figure 4 and online movie). During the first phase (H II-region-dominated phase; from year 3 to 15) the fastest ejecta interact with the H II region and the X-ray emission is dominated by shocked plasma from this region and by a smaller contribution from the outermost ejecta (see Figures 5, 6, and online movie). In the second phase (ring-dominated phase; from year 15 to 32) the ejecta interacts with the dense equatorial ring. The emission in the soft X-ray band is largely dominated by the shocked clumps (see Figures 5, 6, and online movie). The emission in the hard X-ray band is mainly due to shocked plasma from the smooth component of the ring and to fragments of the shocked clumps stripped by hydrodynamic instabilities developing at the cloud boundaries. In the third phase (ejecta-dominated phase; from year 32), the forward shock propagates beyond the majority of the dense ring material and the reverse shock travels through the inner envelope of the SN. The X-ray emission is dominated by shocked ejecta (see Figures 5 and 6) and the remnant morphology is characterized by very bright knots due to shocked clumps of ejecta (see online movie).

2. Our favored model reproduces the main observables of SN 1987A (i.e., bolometric lightcurve, evolution of photospheric temperature, and velocity) during the first 250 days after explosion and the observed X-ray lightcurves and spectra of its remnant (see Figures 5 and 6) in the following 30 years. Therefore, we have demonstrated that the physical model reproducing the observables of the SN is also able to reproduce the observables of the subsequent expanding remnant, providing a firm link between two research fields (SN explosions and SNR evolution) that, traditionally, are based on models that are independent from each other. In other words, in the case of SN 1987A, we have demonstrated the consistency between the cause (the SN explosion) and the effect (the interaction of the remnant with the surrounding medium). This is a great advance with respect to a parameterized explosion model to bootstrap the SNR (as those commonly used in the literature) whose parameters are chosen to fit the observables of the remnant but do not ensure the fit to the observables of the progenitor SN as well.

3. From our favored model, we identified the imprint of SN 1987A on the remnant emission. In particular, we constrained the SN explosion energy in the range  $1.2\text{--}1.4 \times 10^{51}$  erg and the envelope mass in the range  $15\text{--}17 M_{\odot}$ . The model also constrained the physical properties of post-explosion ejecta. During the H II-region-dominated phase, the sudden increase of X-ray flux observed around year 4 (Figure 5(b)) is reproduced if the outermost ejecta have a post-explosion radial profile of density approximated by a power law with index  $\alpha = -8$ . On the contrary, models with

index  $\alpha = -9$  (as initially suggested for SN 1987A; Woosley 1988) systematically underestimate the soft X-ray flux during the first seven years after the explosion (see Figure 9), independently of the density structure of the nebula within the range of values compatible with observations. Indeed, the shape of the lightcurves in this phase reflect the structure of outer ejecta and reveal the imprint of the SN on the remnant emission.

4. Our favored model allowed us to constrain the structure of the pre-SN nebula. In the ring-dominated phase, the shape of the lightcurves and spectra reflect the density structure of the nebula, allowing us to disentangle the effects of the SN event (identified in the previous phase) from those of the remnant interaction with the environment. This enabled us to ascertain the origin of the multi-thermal X-ray emission and to constrain the nebula structure (see Table 1 for all the details). From this model, we estimated that the total mass of the ring is  $M_{\text{rg}} = 0.062 M_{\odot}$ , of which  $\sim 64\%$  is plasma with density  $n \approx 1000 \text{ cm}^{-3}$  and  $\sim 36\%$  is plasma with  $n \approx 2.5 \times 10^4 \text{ cm}^{-3}$ . These values are in excellent agreement with those derived from optical spectroscopic data for the density structure of the ionized gas of the ring (Mattila et al. 2010).

Our model enabled us to make predictions about the ejecta evolution and the future changes in the remnant morphology in X-rays. In the next few years, the remnant will enter in the ejecta-dominated phase. The X-ray flux will reflect the radial profile of density in outer ejecta: the steeper the slope of this profile, the higher the emission from shocked ejecta. The emission will enable us to study in more detail the ejecta asymmetries and the distribution of metal-rich layers. This will provide important clues on the dynamics of the explosion and might even improve our knowledge about the nucleosynthesis processes occurring in the latest stage of stellar evolution and during the SN explosion, making the remnant of SN 1987A a unique probe of CC-SNe.

Finally, we investigated how our model relates to the existence of the yet undetected central compact remnant. The complete picture of the line of sight column toward the center of SN 1987A provided by our model has shown that the emission of the compact remnant cannot be revealed yet due to a local absorbing column density that is a factor of 20 higher than the interstellar absorption toward the Large Magellanic Cloud. The constraint on the thermal emission from the central source inferred from our model is in good agreement with standard theories of neutron star cooling.

We thank Roger Chevalier, Dan Dewey, Fabio Reale, and Salvo Sciortino for helpful discussions. We also thank the anonymous referee for useful suggestions that we have incorporated into the paper. This paper was partially funded by the PRIN INAF 2014 grant. MLP acknowledges financial support from CSFNSM and from INAF. The software used in this work was, in part, developed by the U.S. Department of Energy supported Advanced Simulation and Computing/Alliance Center for Astrophysical Thermonuclear Flashes at the University of Chicago. We acknowledge that the results of this research have been achieved using the PRACE Research Infrastructure resource MareNostrum III based in Spain at the Barcelona Supercomputing Center (PRACE Award N.2012060993). We acknowledge the CINECA Award N. HP10B136DG,2012 for the availability of high performance computing resources and support.

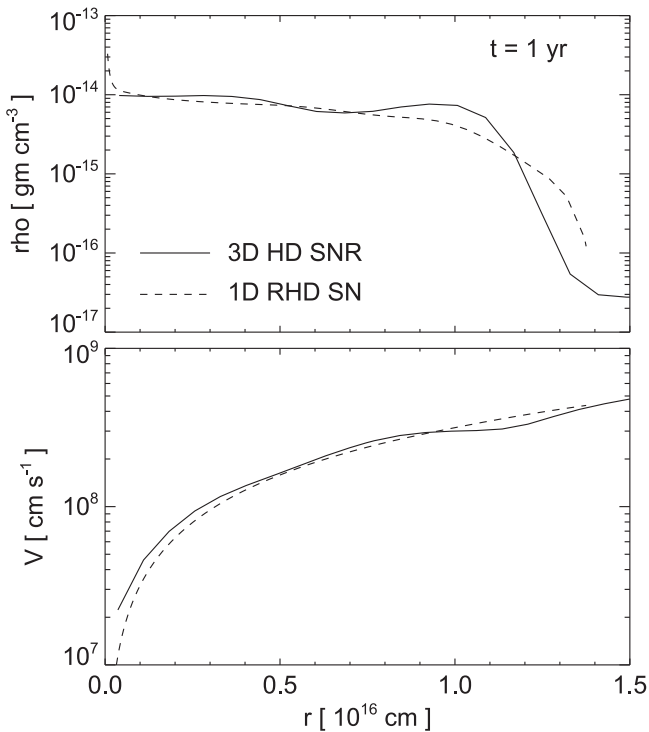


**Figure 11.** Radial profiles of the mass density (upper panel) and velocity (lower panel) of the ejecta at  $t = 1$  year since the SN event. The solid curves show the angle-averaged profiles derived with the 3D hydrodynamic model describing the SNR evolution; the dashed curves show the analogous profiles derived with the 1D relativistic radiation hydrodynamic code describing the post-explosion evolution of the SN.

## APPENDIX A

### EFFECT OF RADIOACTIVE HEATING DURING THE REMNANT EXPANSION

The 3D hydrodynamic simulations describing the evolution of the SNR and its interaction with the inhomogeneous CSM do not include a heating term due to decays of radioactive isotopes synthesized in the SN explosion (e.g.,  $^{56}\text{Co}$  or  $^{44}\text{Ti}$ ). To check the validity of our assumption, we used our 1D relativistic radiation hydrodynamic code (which includes the radioactive heating term; see Section 2.1), to extend run SN-M17-E1.2-N8, simulating the post-explosion evolution of the SN and covering the first year of evolution. Then we compared the radial profiles of the mass density and velocity of ejecta derived in this case at  $t = 1$  year with the angle-averaged radial profiles of density and velocity derived at the same epoch with our 3D hydrodynamic model (not including the radioactive heating). Figure 11 shows some differences in the density profiles that are mainly due to the effect of ejecta clumping considered only in the 3D simulation. On the other hand, the two velocity profiles are very similar, suggesting that the effect of radioactive heating does not affect the dynamics of the ejecta too much. This result suggests that we can safely neglect the effect of radioactive heating during the interaction of the remnant with the surrounding nebula.

## APPENDIX B

### THE DATA ANALYSIS

We present new results of the analysis of different observations of the remnant of SN 1987A performed with the *ASCA*, *XMM-Newton*, and *Chandra* X-ray telescopes. We

adopted Xselect V2.4, CIAO V4.6.1, and SAS V13 for the reduction of *ASCA*/SIS, *XMM-Newton*/EPIC, and *Chandra*/ACIS data, respectively. All the spectra were analyzed with XSPEC V12.8.2.

### B.1. ASCA Data

We analyzed the *ASCA* observations ID 55039000 (performed in 1997 November), 56041000 (1998 November), and 57034000 (1999 November) to derive the X-ray unabsorbed fluxes in the [0.5, 2] keV and [3, 10] keV bands, as shown in Figure 5. We screened the data according to the standard screening criteria and added the screened SIS0 and SIS1 spectra by using the ADDASCASPEC task. We verified that the spectra extracted from observations 55039000 and 56041000 were consistent with each other, considering the relatively low signal-to-noise ratio of the early observations of SN 1987A. We then fitted the SIS spectra extracted from observations 55039000 and 56041000 simultaneously. For each spectrum, we subtracted a background spectrum extracted from a nearby region immediately outside the SNR shell, and we verified that the best-fit values did not depend significantly on the choice of the background region. Spectra were modeled by an absorbed (TBABS model in XSPEC) optically thin plasma in NEI (VNEI model). In the fittings, the plasma chemical abundances were fixed to the values derived from the analysis of deep *Chandra*/LETG and HETG observations of SN 1987A (Zhekov et al. 2009), while the interstellar column density was fixed to (Park et al. 2006)  $N_{\text{H}} = 2.35 \times 10^{21} \text{ cm}^{-2}$ . Our best-fit models provide a good description of the spectra ( $\chi^2 = 41.5$  with 47 degrees of freedom (dof) for the 1997 and 1998 spectra, and  $\chi^2 = 36.0$  with 29 dof for the 1999 spectrum) and the best-fit temperatures and ionization timescales are  $kT = 1.5 \pm 0.3 \text{ keV}$ ,  $\tau = 3 \pm 2 \times 10^{10} \text{ s cm}^{-3}$  for the 1997 and 1998 spectra and  $kT = 1.7 \pm 0.4 \text{ keV}$ ,  $\tau = 2 \pm 1 \times 10^{10} \text{ s cm}^{-3}$  for the 1999 spectrum.

### B.2. XMM-Newton Data

As for the *XMM-Newton* data, we analyzed observation ID 0083250101 (performed in 2001 April) and the previously unpublished observation ID 0690510101 (performed in 2012 December). We focused on the EPIC data and selected events with PATTERN  $\leq 12$  for the MOS cameras, PATTERN  $\leq 4$  for the pn camera, and FLAG = 0 for both. We screened the original event files by using the sigma-clipping algorithm (ESPFILT tasks). The pn spectra extracted from the 2001/2012 observations are shown in the upper/middle panels of Figure 6. To derive the [0.5, 2] keV and [3, 10] keV fluxes of the 2012 observation, we fitted the pn and MOS spectra simultaneously (selecting a circular extraction region with radius  $r = 20''$ ) in the [0.3, 9] keV energy band. We adopted a model including three components of optically thin plasma in NEI, which are widely used (Maggi et al. 2012) to describe the latest X-ray observations of SN 1987A. Again we fixed the interstellar column density (Park et al. 2006) to  $N_{\text{H}} = 2.35 \times 10^{21} \text{ cm}^{-2}$ . The chemical abundances were fixed to the values derived in previous studies (Zhekov et al. 2009) for all the three components. The best-fit temperatures are  $kT_1 = 0.48^{+0.01}_{-0.02} \text{ keV}$ ,  $kT_2 = 0.77 \pm 0.03 \text{ keV}$ , and  $kT_3 = 2.41 \pm 0.05 \text{ keV}$ , while the corresponding ionization timescales are  $\tau_1 = 1.5 \pm 0.1 \times 10^{11} \text{ s cm}^{-3}$ ,  $\tau_2 = 2.4 \pm 0.3 \times 10^{13} \text{ s cm}^{-3}$ ,

and  $\tau_3 = 1.11_{-0.03}^{+0.05} \times 10^{11} \text{ s cm}^{-3}$ . The presence of a component with a  $\tau > 10^{13} \text{ s cm}^{-3}$  (in our case, component 2) indicates that part of the X-ray emitting plasma has reached the collisional ionization equilibrium, and is in agreement with previous findings (Helder et al. 2013). We point out that these models only provide heuristic (phenomenological) descriptions of the spectra, whose physical origin can be unveiled only by accurate hydrodynamic modeling (see Section 3.2).

### B.3. Chandra Data

Finally, we analyzed the *Chandra*/ACIS observation 1967 (performed on 2000 December) and the previously unpublished observation 14697 (2013 March) to produce the X-ray images shown in Figure 4 (lower panels). To study the morphology of SN 1987A from the observations, we carefully followed the procedure described in the literature (Burrows et al. 2000; Park et al. 2002). The ACIS data were deconvolved with a maximum likelihood algorithm (with 25 iterations; Richardson 1972; Lucy 1974), using an on-axis point-spread function produced by the MARX simulation package. The high photon statistics allowed us to use  $0''.062$  pixels for the deconvolution process. The deconvolved images were finally smoothed with a Gaussian with  $\sigma = 0''.1$ .

## REFERENCES

- Anders, E., & Grevesse, N. 1989, *GeCoA*, **53**, 197
- Arnett, D. 1996, *Supernovae and Nucleosynthesis: An Investigation of the History of Matter from the Big Bang to the Present* (Princeton, NJ: Princeton Univ. Press)
- Arnett, W. D. 1987, *ApJ*, **319**, 136
- Arnett, W. D., Bahcall, J. N., Kirshner, R. P., & Woosley, S. E. 1989, *ARA&A*, **27**, 629
- Badenes, C., Hughes, J. P., Cassam-Chenaï, G., & Bravo, E. 2008, *ApJ*, **680**, 1149
- Bersten, M. C., Benvenuto, O., & Hamuy, M. 2011, *ApJ*, **729**, 61
- Blinnikov, S., Lundqvist, P., Bartunov, O., Nomoto, K., & Iwamoto, K. 2000, *ApJ*, **532**, 1132
- Burrows, D. N., Michael, E., Hwang, U., et al. 2000, *ApJL*, **543**, L149
- Catchpole, R. M., Menzies, J. W., Monk, A. S., et al. 1987, *MNRAS*, **229**, 15P
- Catchpole, R. M., Whitelock, P. A., Feast, M. W., et al. 1988, *MNRAS*, **231**, 75P
- Chevalier, R. A., & Dwarkadas, V. V. 1995, *ApJL*, **452**, L45
- Chita, S. M., Langer, N., van Marle, A. J., García-Segura, G., & Heger, A. 2008, *A&A*, **488**, L37
- Colella, P., & Woodward, P. R. 1984, *JCoPh*, **54**, 174
- Crotts, A. P. S., Kunkel, W. E., & McCarthy, P. J. 1989, *ApJL*, **347**, L61
- Dall’Ora, M., Botticella, M. T., Pumo, M. L., et al. 2014, *ApJ*, **787**, 139
- Dewey, D., Dwarkadas, V. V., Haberl, F., Sturm, R., & Canizares, C. R. 2012, *ApJ*, **752**, 103
- Dwarkadas, V. V., Dewey, D., & Bauer, F. 2010, *MNRAS*, **407**, 812
- Dwek, E., Arendt, R. G., Bouchet, P., et al. 2010, *ApJ*, **722**, 425
- Ellinger, C. I., Young, P. A., Fryer, C. L., & Rockefeller, G. 2012, *ApJ*, **755**, 160
- Fransson, C., & Chevalier, R. A. 1987, *ApJL*, **322**, L15
- Fryxell, B., Olson, K., Ricker, P., et al. 2000, *ApJS*, **131**, 273
- Gaensler, B. M., Manchester, R. N., Staveley-Smith, L., et al. 1997, *ApJ*, **479**, 845
- Ghavamian, P., Laming, J. M., & Rakowski, C. E. 2007, *ApJL*, **654**, L69
- Haberl, F., Geppert, U., Aschenbach, B., & Hasinger, G. 2006, *A&A*, **460**, 811
- Hamilton, A. J. S., Sarazin, C. L., & Chevalier, R. A. 1983, *ApJS*, **51**, 115
- Hamuy, M., Suntzeff, N. B., Gonzalez, R., & Martin, G. 1988, *AJ*, **95**, 63
- Handy, T., Plewa, T., & Odrzywołek, A. 2014, *ApJ*, **783**, 125
- Hasinger, G., Aschenbach, B., & Truemper, J. 1996, *A&A*, **312**, L9
- Helder, E. A., Broos, P. S., Dewey, D., et al. 2013, *ApJ*, **764**, 11
- Hole, K. T., Kasen, D., & Nordsieck, K. H. 2010, *ApJ*, **720**, 1500
- Joggerst, C. C., Woosley, S. E., & Heger, A. 2009, *ApJ*, **693**, 1780
- Kjær, K., Leibundgut, B., Fransson, C., Jerkstrand, A., & Spyromilio, J. 2010, *A&A*, **517**, A51
- Kwok, S., Purton, C. R., & Fitzgerald, P. M. 1978, *ApJL*, **219**, L125
- Larsson, J., Fransson, C., Kjær, K., et al. 2013, *ApJ*, **768**, 89
- Larsson, J., Fransson, C., Óstlin, G., et al. 2011, *Natur*, **474**, 484
- Lawrence, S. S., Sugerman, B. E., Bouchet, P., et al. 2000, *ApJL*, **537**, L123
- Löhner, R. 1987, *CMAME*, **61**, 323
- Lucy, L. B. 1974, *AJ*, **79**, 745
- Maggi, P., Haberl, F., Sturm, R., & Dewey, D. 2012, *A&A*, **548**, L3
- Mattila, S., Lundqvist, P., Gröningsson, P., et al. 2010, *ApJ*, **717**, 1140
- McCray, R. 2007, in *AIP Conf. Ser. 937, Supernova 1987A: 20 Years After: Supernovae and Gamma-Ray Bursters*, ed. S. Immler, K. Weiler & R. McCray (Melville, NY: AIP), **3**
- Morris, T., & Podsiadlowski, P. 2007, *Sci*, **315**, 1103
- Nandra, K., Barret, D., Barcons, X., et al. 2013, arXiv:1306.3307
- Ng, C.-Y., Gaensler, B. M., Murray, S. S., et al. 2009, *ApJL*, **706**, L100
- Orlando, S., Bocchino, F., Miceli, M., Petruk, O., & Pumo, M. L. 2012, *ApJ*, **749**, 156
- Orlando, S., Bocchino, F., Peres, G., et al. 2006, *A&A*, **457**, 545
- Orlando, S., Drake, J. J., & Laming, J. M. 2009, *A&A*, **493**, 1049
- Panagia, N. 1999, in *IAU Symp. 190, New Views of the Magellanic Clouds*, ed. Y.-H. Chu et al. (Cambridge: Cambridge Univ. Press), **539**
- Park, S., Burrows, D. N., Garmire, G. P., et al. 2002, *ApJ*, **567**, 314
- Park, S., Zhekov, S. A., Burrows, D. N., & McCray, R. 2005, *ApJL*, **634**, L73
- Park, S., Zhekov, S. A., Burrows, D. N., et al. 2006, *ApJ*, **646**, 1001
- Pastorello, A., Pumo, M. L., Navasardyan, H., et al. 2012, *A&A*, **537**, A141
- Patnaude, D. J., Lee, S.-H., Slane, P. O., et al. 2015, *ApJ*, **803**, 101
- Phillips, M. M., Heathcote, S. R., Hamuy, M., & Navarrete, M. 1988, *AJ*, **95**, 1087
- Potter, T. M., Staveley-Smith, L., Reville, B., et al. 2014, *ApJ*, **794**, 174
- Pumo, M. L., & Zampieri, L. 2011, *ApJ*, **741**, 41
- Pumo, M. L., & Zampieri, L. 2013, *MNRAS*, **434**, 3445
- Richardson, W. H. 1972, *JOSA*, **62**, 55
- Shigeyama, T., & Nomoto, K. 1990, *ApJ*, **360**, 242
- Shternin, P. S., & Yakovlev, D. G. 2008, *AstL*, **34**, 675
- Smith, N., Arnett, W. D., Bally, J., Ginsburg, A., & Filippenko, A. V. 2013, *MNRAS*, **429**, 1324
- Smith, R. K., Brickhouse, N. S., Liedahl, D. A., & Raymond, J. C. 2001, *ApJL*, **556**, L91
- Spiro, S., Pastorello, A., Pumo, M. L., et al. 2014, *MNRAS*, **439**, 2873
- Sugerman, B. E. K., Crotts, A. P. S., Kunkel, W. E., Heathcote, S. R., & Lawrence, S. S. 2005, *ApJS*, **159**, 60
- Takáts, K., Pumo, M. L., Elias-Rosa, N., et al. 2014, *MNRAS*, **438**, 368
- Utrobin, V. P., & Chugai, N. N. 2005, *A&A*, **441**, 271
- Wang, L., Baade, D., Höflich, P., Wheeler, J. C., Kawabata, K., & Nomoto, K. 2004, *ApJL*, **604**, L53
- Wang, L., Baade, D., Höflich, P., et al. 2003, *ApJ*, **591**, 1110
- West, R. M., Lauberts, A., Schuster, H.-E., & Jorgensen, H. E. 1987, *A&A*, **177**, L1
- Wilms, J., Allen, A., & McCray, R. 2000, *ApJ*, **542**, 914
- Woosley, S. E. 1988, *ApJ*, **330**, 218
- Yakovlev, D. G., & Pethick, C. J. 2004, *ARA&A*, **42**, 169
- Yamaguchi, H., Badenes, C., Petre, R., et al. 2014, *ApJL*, **785**, L27
- Young, T. R. 2004, *ApJ*, **617**, 1233
- Zhekov, S. A., McCray, R., Dewey, D., et al. 2009, *ApJ*, **692**, 1190